PNAS PLUS

An oligotrophic deep-subsurface community dependent on syntrophy is dominated by sulfur-driven autotrophic denitrifiers

Maggie C. Y. Lau[a,1], Thomas L. Kieft[b], Olukayode Kuloyo[c,2], Borja Linage-Alvarez[c,3], Esta van Heerden[c], Melody R. Lindsay[a,4], Cara Magnabosco[a,5], Wei Wang[d], Jessica B. Wiggins[d], Ling Guo[d], David H. Perlman[e,6], Saw Kyin[e], Henry H. Shwe[e], Rachel L. Harris[a], Youmi Oh[f,7], Min Joo Yi[g], Roland Purtschert[h], Greg F. Slater[i], Shuhei Ono[j], Siwen Wei[k], Long Li[k,l], Barbara Sherwood Lollar[l], and Tullis C. Onstott[a]

[a]Department of Geosciences, Princeton University, Princeton, NJ 08544; [b]Department of Biology, New Mexico Institute of Mining and Technology, Socorro, NM 87801; [c]Department of Microbial, Biochemical, and Food Biotechnology, University of the Free State, Bloemfontein 9301, South Africa; [d]High Throughput Sequencing and Microarray Facility, Lewis–Sigler Institute for Integrative Genomics, Princeton University, NJ 08544; [e]Proteomics and Mass Spectrometry Core, Department of Molecular Biology, Princeton University, NJ 08544; [f]Atmospheric and Oceanic Sciences, Princeton University, Princeton, NJ 08544; [g]Department of Ecology and Evolutionary Biology, Princeton University, Princeton, NJ 08544; [h]Climate and Environmental Physics, Physics Institute, University of Bern, 3012 Bern, Switzerland; [i]School of Geography and Earth Sciences, McMaster University, Hamilton, ON, Canada L8S 4K1; [j]Department of Earth, Atmospheric, and Planetary Sciences, Massachusetts Institute of Technology, Cambridge, MA 02139; [k]Department of Earth and Atmospheric Sciences, University of Alberta, Edmonton, AB, Canada T6G 2E3; and [l]Department of Earth Sciences, University of Toronto, Toronto, ON, Canada M5S 3B1

Edited by David M. Karl, University of Hawaii, Honolulu, HI, and approved October 26, 2016 (received for review August 10, 2016)

Subsurface lithoautotrophic microbial ecosystems (SLiMEs) under oligotrophic conditions are typically supported by H_2. Methanogens and sulfate reducers, and the respective energy processes, are thought to be the dominant players and have been the research foci. Recent investigations showed that, in some deep, fluid-filled fractures in the Witwatersrand Basin, South Africa, methanogens contribute <5% of the total DNA and appear to produce sufficient CH_4 to support the rest of the diverse community. This paradoxical situation reflects our lack of knowledge about the in situ metabolic diversity and the overall ecological trophic structure of SLiMEs. Here, we show the active metabolic processes and interactions in one of these communities by combining metatranscriptomic assemblies, metaproteomic and stable isotopic data, and thermodynamic modeling. Dominating the active community are four autotrophic β-proteobacterial genera that are capable of oxidizing sulfur by denitrification, a process that was previously unnoticed in the deep subsurface. They co-occur with sulfate reducers, anaerobic methane oxidizers, and methanogens, which each comprise <5% of the total community. Syntrophic interactions between these microbial groups remove thermodynamic bottlenecks and enable diverse metabolic reactions to occur under the oligotrophic conditions that dominate in the subsurface. The dominance of sulfur oxidizers is explained by the availability of electron donors and acceptors to these microorganisms and the ability of sulfur-oxidizing denitrifiers to gain energy through concomitant S and H_2 oxidation. We demonstrate that SLiMEs support taxonomically and metabolically diverse microorganisms, which, through developing syntrophic partnerships, overcome thermodynamic barriers imposed by the environmental conditions in the deep subsurface.

active subsurface environment | metabolic interactions | sulfur-driven autotrophic denitrifiers | syntrophy | inverted biomass pyramid

Microorganisms living in deep-subsurface ecosystems acquire energy through chemosynthesis and carbon from organic or inorganic sources. Whereas heterotrophs use dissolved organic carbon (DOC) transported from the surface and/or produced in situ, detrital organic deposits buried along with the sediments, and hydrocarbons migrating into petroleum reservoirs, chemolithoautotrophs fix dissolved inorganic carbon (DIC). In oligotrophic systems, subsurface lithoautotrophic microbial ecosystems (SLiMEs) (1) that are fueled by H_2 support the occurrence of autotrophic methanogens, acetogens, and sulfate reducers (2–5). These environments can host highly diverse communities, consisting mostly of prokaryotes, but also multicellular microeukaryotes and viral particles (6–13). Due to the limitation of available nutrients and energy substrates in the oligotrophic subsurface, it is reasonable to hypothesize that subsurface inhabitants with diverse functional traits cooperate syntrophically to maximize energy yield

Significance

Microorganisms are known to live in the deep subsurface, kilometers below the photic zone, but the community-wide metabolic networks and trophic structures (the organization of their energy and nutritional hierarchy) remain poorly understood. We show that an active subsurface lithoautotrophic microbial ecosystem (SLiME) under oligotrophic condition exists. Taxonomically and metabolically diverse microorganisms are supported, with sulfur-driven autotrophic denitrifiers predominating in the community. Denitrification is a highly active process in the deep subsurface that evaded recognition in the past. This study highlights the critical role of metabolic cooperation, via syntrophy between subsurface microbial groups, for the survival of the whole community under the oligotrophic conditions that dominate in the subsurface.

Author contributions: M.C.Y.L. and T.C.O. designed research; M.C.Y.L., C.M., W.W., and T.C.O. planned the technical approach of metatranscriptomics; M.C.Y.L., D.H.P., and T.C.O. planned the technical approach of metaproteomics; M.C.Y.L., T.L.K., O.K., B.L.-A., E.v.H., M.R.L., C.M., W.W., J.B.W., L.G., D.H.P., S.K., H.H.S., R.P., G.F.S., S.O., S.W., L.L., B.S.L., and T.C.O. performed research; E.v.H. was the point of contact with the mining company; M.C.Y.L., T.L.K., O.K., B.L.-A., E.v.H., M.R.L., and C.M. collected samples; M.C.Y.L., M.R.L., R.L.H., Y.O., M.J.Y., R.P., G.F.S., S.O., S.W., L.L., B.S.L., and T.C.O. analyzed data; G.F.S., S.O., L.L., B.S.L., and T.C.O. assisted with the interpretation of isotopic data; T.L.K., C.M., W.W., J.B.W., D.H.P., S.K., G.F.S., L.L., B.S.L., and T.C.O. contributed to and/or commented on the earlier drafts of the manuscript; and M.C.Y.L. wrote the paper.

The authors declare no conflict of interest.

This article is a PNAS Direct Submission.

Data deposition: The single-end Illumina reads of the RNA-seq data have been deposited at the National Center for Biotechnology Information BioProject (accession no. PRJNA308990). The Sanger sequences obtained by RT-PCR cloning have been deposited in the GenBank database (accession nos. KF901390–KF901421 and KF901484–KF901489). The mass spectrometry proteomics data have been deposited to the ProteomeXchange Consortium via the PRIDE partner repository (dataset identifier PXD004634).

[1]To whom correspondence should be addressed. Email: maglau@princeton.edu.

[2]Present address: Energy Bioengineering and Geomicrobiology Group, University of Calgary, Calgary, AB, Canada T2N 1N4.

[3]Present address: Consorcio de Promoción del Ovino, 49630 Villalpando, Castillo-León, Spain.

[4]Present address: Department of Microbiology and Immunology, Montana State University, Bozeman, MT 59717.

[5]Present address: Simons Center for Data Analysis, Simons Foundation, New York, NY 10010.

[6]Present address: Department of Chemistry, Princeton University, NJ 08544.

[7]Present address: Department of Earth, Atmospheric, and Planetary Sciences, Purdue University, West Lafayette, IN 47907.

This article contains supporting information online at www.pnas.org/lookup/suppl/doi:10.1073/pnas.1612244113/-/DCSupplemental.

and growth, as has been demonstrated elsewhere (14–16). How such interspecies metabolic interactions relate to the subsurface trophic structure remains largely unexplored.

Syntrophy refers to metabolic partners being dependent on each other to create better conditions that are mutually beneficial for the metabolic activities observed (14), and critically, "the mutual dependence cannot be overcome by simply adding a cosubstrate or any type of nutrient" (16). Syntrophic microbial consortia are well known to anaerobically degrade organic carbon by cross-feeding on metabolic products such as acetate, formate, and H_2 such that these substances do not accumulate to a toxic level that could suppress the activity of the producers (16). Anaerobic methane oxidizers (ANMEs) and sulfate reducers are the syntrophic partners responsible for anaerobic CH_4 oxidation in shallow, anoxic CH_4-rich sediments. The details of such metabolic interaction are not fully understood but it is now known to involve production of S^0 by ANMEs as an intermediate (17) and/or nanowires for direct electron transfer (18, 19). Recently, a consortium of *Thioploca* and anaerobic ammonia oxidizers that uses NO_3^- and NH_4^+ as the electron-shuttling system was shown to contribute significantly to the loss of organic nitrogen in continental margin sediments at much shallower depths (20). It is, however, yet to be determined whether this partnership is commensal or syntrophic. Regardless, the latter two examples from oceanic subsurface environments validate the idea that symbiosis among microorganisms (via obligate and facultative syntrophy, mutualism, and commensalism) could play a pivotal role in sustaining the microbiome and biogeochemical cycling in the deeper biosphere on the Earth.

Our recent investigations in the Witwatersrand Basin, South Africa, indicated that the H_2-driven microbial groups (methanogens, acetogens, and sulfate reducers) are less prevalent in the DNA communities (21) than previously perceived (2, 4, 22). Interestingly, in some cases, methanogens comprising <5% of the total DNA apparently produce sufficient CH_4 to support the rest of the community (23). These results indicate that our understanding of the metabolisms and energy fluxes in SLiMEs is far from complete (24). This study aimed to test the hypotheses that methanogenesis and/or other H_2-driven processes are the predominant primary producers in SLiMEs and that methanogenic CH_4 from the rare methanogenic population sustains the entire community. Here, we describe the active community and metabolic pathways in fracture fluid with relatively low DOC (28.8 μM) (21, 23). We used metatranscriptomics and metaproteomics to map the metabolic landscape of the active microbial community and to decipher the metabolic network among members. Our results show that this oligotrophic ecosystem runs upon syntrophic cooperation between microbial groups and is dominated by sulfur-oxidizing, autotrophic, denitrifying bacteria.

Results and Discussion

Geochemistry Characterization. The fluid investigated was collected from a fault zone at 1.34-km depth in the Witwatersrand Basin, South Africa. It was warm (38 °C), alkaline (pH 8.6), brackish (total dissolved solids, 3.6 $g{\cdot}L^{-1}$) and hypoxic (pe = −1.4) (21, 23) (*SI Appendix*, Table S1). It had low H_2 (8.9 nM), high CH_4 (1.3 mM) relative to DIC (330 μM), and high SO_4^{2-} (623 μM) relative to HS^- (14.9 μM). Noble gas-derived residence time for the fracture water (3–14 my based on ^{40}Ar, ^{134}Xe, and ^{136}Xe), and radiocarbon ages of 40–80 ky for the DIC in the water indicate mixing of older fracture water trapped in the Witwatersrand host rocks and paleometeoric waters sourcing the DIC (12, 25–27) (*SI Appendix*, Table S1).

Molecular Analyses. We extracted the community DNA, RNA, and protein in parallel from biomass captured on a 0.1-μm-pore size membrane filter. The DNA community was dominated by Proteobacteria, with metabolic potential for methanogenesis, CH_4 oxidation, SO_4^{2-} reduction, NO_3^- reduction, and N_2 fixation (8, 21, 23). This study analyzed the RNA and protein samples using metatranscriptomics and metaproteomics, respectively. High-quality single-end reads, a total of 21,577,391 bp, were generated from the total RNA (*SI Appendix*, Table S2). Protein-encoding genes (PEGs) predicted from assembled mRNA transcripts were then used to annotate the metaproteome, and 1,983 unique peptides representing 824 protein IDs were identified. As mRNAs and proteins have different response times to environmental changes (28), they provide independent yet complementary snapshots of the active metabolic landscape. Relative abundances of active microorganisms reported here are derived from ribosomal RNA (rRNA) transcripts ($\%_{rRNA}$) and ribosomal protein PEGs ($\%_{rp}$). Because the per-cell abundance of these molecules varies, these values may not be directly equivalent to biomass, but they provide a reasonable approximation.

Taxonomic Diversity. Proteobacteria (85.3$\%_{rRNA}$ and 73.6$\%_{rp}$) significantly outnumbered 38 other microbial phyla detected in the fracture fluid sample at the time of collection (*SI Appendix*, Fig. S1). Archaea comprised only 1.9$\%_{rRNA}$ and <0.1$\%_{rp}$, and eukaryotes were negligible (0.03$\%_{rRNA}$) (*SI Appendix*, Fig. S1). This taxonomic profile of the active microbial (RNA) community is very similar to that of the total DNA community derived from the same sample (8, 21, 23). The active members will be described in greater detail along with the results of the expressed gene and enzymes for the N, S, and C metabolisms.

Nitrogen Metabolisms. The occurrence of canonical denitrification is indicated by detection of a complete suite of PEGs and the encoded enzymes (Fig. 1), and the metabolic intermediate N_2O (22 μM; *SI Appendix*, Table S1). Diverse denitrifiers related to *Sulfuritalea* (0.3$\%_{rRNA}$ and 20.1$\%_{rp}$) and *Thauera* (1.5$\%_{rRNA}$ and 3.5$\%_{rp}$) of Rhodocyclaceae (25.7$\%_{rRNA}$ and 39.4$\%_{rp}$), *Thiobacillus* (3.3$\%_{rRNA}$ and 2.3$\%_{rp}$) and *Sulfuricella* (0.2$\%_{rRNA}$ and 1.8$\%_{rp}$) of Hydrogenophilaceae (4.7$\%_{rRNA}$ and 5.0$\%_{rp}$), Rhodospirillaceae (4.3$\%_{rRNA}$ and 2.9$\%_{rp}$), Ectothiorhodospiraceae (1.7$\%_{rRNA}$ and 1.5$\%_{rp}$), and Bacillaceae (0.3$\%_{rRNA}$) were detected.

The discrepancy between the relative abundances of *Sulfuritalea*-like taxa in rRNA transcripts and ribosomal protein PEGs was further investigated. About 70% of the rRNA transcripts cannot be assigned to known β-proteobacterial Rhodocyclaceae genera, whereas 50% of the ribosomal protein PEGs are related to *Sulfuritalea* (*SI Appendix*, Fig. S2). Reciprocal best-hit (RBH) BLAST search between the complete PEG transcriptome and 21 published Rhodocyclaceae genomes provides independent support of *Sulfuritalea*'s dominance (*SI Appendix*, Fig. S2). The RBH BLAST search also indicates that *Sulfuritalea*- and *Thauera*-like taxa expressed PEGs involved in canonical denitrification, sulfur (HS^-, S^0, $S_2O_3^{2-}$, SO_3^{2-}) oxidation, and the Calvin–Benson–Bassham (CBB) cycle (green-outlined in Fig. 1; *SI Appendix*, Table S3). Together with *Thiobacillus*- and *Sulfuricella*-like taxa, sulfur-driven autotrophic denitrifiers (autotrophic microorganisms that couple NO_3^- reduction with sulfur oxidation) accounted for 27.8$\%_{rp}$ of the active community.

In addition to canonical denitrification, NO_2^- removal via anaerobic ammonium oxidation (ANAMMOX) and dissimilatory nitrate reduction to ammonia (DNRA) are indicated by the detection of the key enzymes Planctomycetes-related nitrite reductase (NirS) and hydroxylamine oxidoreductase (HAO) for ANAMMOX, and cytochrome *c* nitrite reductase (ccNIR) for DNRA, respectively. Brocadiaceae capable of ANAMMOX constituted only 0.07% of the rRNA. By RT-PCR cloning, we retrieved *nif*H gene transcripts of uncultured Proteobacteria in the same fracture fluid (*SI Appendix*, Table S4), indicating that microbial fixation of N_2 occurred, but likely at levels too low to be detected in the PEG transcriptome. The highly isotopically enriched NO_3^- ($\delta^{15}N_{AIR} = 36.3 \pm 0.1‰$; $\delta^{18}O_{VSMOW} = 49.2 \pm 0.5‰$), along with the relative $\delta^{15}N$ depletion in N_2 ($\delta^{15}N_{AIR} = -1$ ‰) observed in this sample (*SI Appendix*, Table S1) are consistent with canonical denitrification as the principal N pathway (Fig. 2) (29). The NO_3^- may originate from radiolytic oxidation of NH_3/NH_4^+ in the rock formation pore water (29) and/or from paleometeoric recharge (as for the DIC). The denitrifiers appear to have reduced NO_3^- to trace levels (0.3 μM).

Sulfur Metabolisms. For sulfur-driven autotrophic denitrification to take place, *Sulfuritalea*- and *Sulfuricella*-like taxa need the electron donors S^0 and $S_2O_3^{2-}$ (30, 31), whereas *Thiobacillus*- and

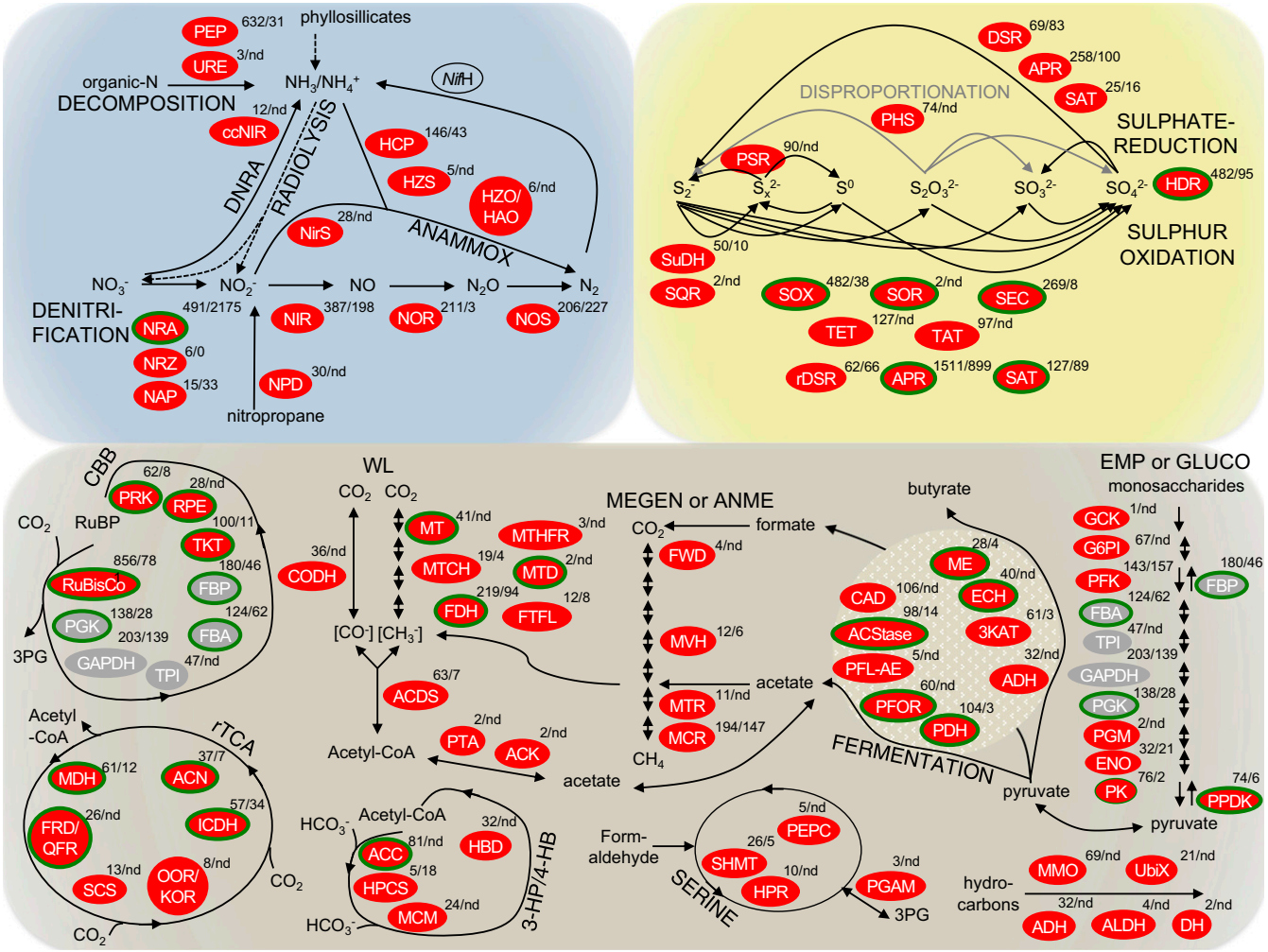

Fig. 1. Metabolic pathways expressed in the deep subsurface. Pathways of N, S, and C metabolisms are enclosed in blue, yellow, and brown envelopes, respectively. Black and gray solid lines indicate reactions mediated by enzymes, whereas black dotted lines in the N cycle indicate abiotic reactions. PEG transcripts and the encoded enzymes detected in this study are denoted by ellipses, appended with coverage (mapped read counted normalized to PEG transcript length) and, if detected, the number of peptide spectral matches in metaproteome. Green-outlined enzymes are encoded by PEG transcripts related to *Sulfuritalea* and *Thauera*. Enzymes in gray operate in both autotrophic and heterotrophic C metabolisms, and the PEG transcripts detected in this study were closely related to those of autotrophs and heterotrophs. *Nif*H gene, encoding for dinitrogenase reductase subunit H, was detected by RT-PCR cloning (*SI Appendix, SI Materials and Methods*, Table S4). A complete list of proteins detected in the PEG transcriptome and metaproteome is provided in *SI Appendix*, Table S6. ANAMMOX, anaerobic ammonium oxidation; ANME, anaerobic methane oxidation (upward direction); CBB, Calvin–Benson–Bassham cycle or reductive pentose phosphate cycle; DNRA, dissimilatory nitrate reduction to ammonia; EMP, Embden–Meyerhof–Parnas glycolysis (downward direction); GLUCO, gluconeogenesis (upward direction); 3-HP/4-HB, 3-hydroxypropionate/4-hydroxybutyrate (3-HP/4-HB) cycle; MEGEN, methanogenesis (downward direction); nd, not detected; 3PG, 3-phosphoglycerate; rTCA, reverse tricarboxylic acid cycle; SERINE, formaldehyde assimilation via serine pathway; WL, Wood–Ljundahl or reductive acetyl-CoA pathway.

Thauera-like taxa can also use HS^-. SO_4^{2-} is known to be generated in the deep terrestrial subsurface by oxidation of sulfide-containing minerals in the host rocks by radiolytically produced oxidants (3, 32). Sulfate reduction mediated by sulfate-reducing bacteria (SRB) is then anticipated to provide the reduced S species for sulfur oxidation. Our results reveal a complete sulfuretum, or co-occurrence of sulfur oxidation and sulfate reduction (Fig. 2); yet three lines of evidence support a dominance of sulfur-oxidizing activity. First, multiple sulfur-oxidizing systems were detected, with the key enzymes being expressed at relatively higher levels in both the metatranscriptome and the metaproteome than those for sulfate reduction (Fig. 1). Second, *apr* and *sat* PEGs of sulfur-oxidizing bacteria (SOB) had coverage sixfold and fivefold higher, and the respective proteins APR and SAT of SOB were nine and six times higher, than those belonging to SRB (Fig. 1; *SI Appendix*, Table S5). Third, the dominance of sulfur-oxidizing activity over sulfate-reducing activity is consistent with the observed δ^{34}S-depletion in SO_4^{2-} relative to HS^- ($\delta^{34}S_{VCDT}$ = +4.5‰ vs. +5.9‰) (Fig. 2; *SI Appendix*, Table S1). In an earlier study of fracture water from this same mine, the δ^{34}S values of SO_4^{2-} ranged from +11.1‰ to +20.6‰ and for HS^- from −14.2‰ to −8.4‰, suggesting that sulfate reduction was dominating over sulfur oxidation at that time (33). HS^- concentrations were also ∼100 times greater than that of the present study, although the 16S rRNA gene clone libraries indicated that the SRB were a relatively minor portion of the total bacterial population (33). However, in the present study, the 1.4‰ depletion in the δ_{34}S value SO_4^{2-} falls in the range of 1.3‰ to 4.3‰ observed in laboratory cultures that couple nitrate reduction and sulfide oxidation (34). S flux through SRB must be much lower than that through SOB, thereby supporting the dominance of sulfur-oxidizing activity. All of these results aligned very well with the fact that the SOB (28.3%$_{rp}$, of which 98% are sulfur-driven autotrophic denitrifiers) comprised a larger component of the active microbial community compared with SRB (3%$_{rRNA}$ and 5%$_{rp}$).

Carbon Metabolisms. As described earlier, sulfur-driven autotrophic denitrifiers fix CO_2 via the CBB cycle (green-outlined in Fig. 1;

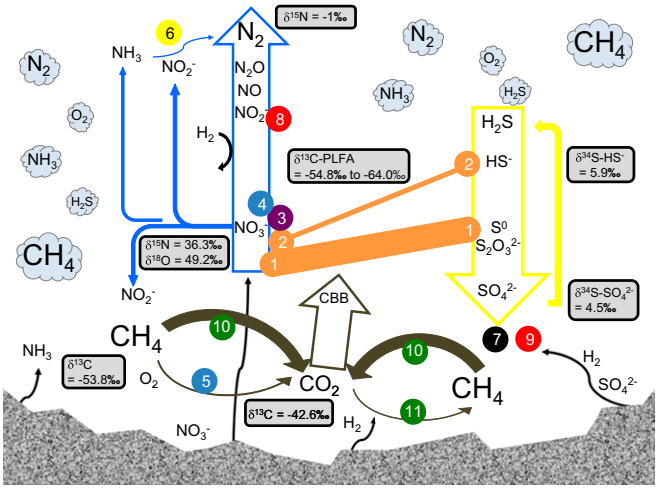

Fig. 2. Metabolic landscape in the deep subsurface. Bubbles represent the gas in the fracture head space, with font size representing the relative abundance of the species. Radiolytic species are originated from the rock. Blue, yellow, and brown arrows, respectively, represent the N, S, and C metabolic pathways detected, with the large arrows representing the principal pathways and the smaller arrows representing the less expressed. CBB stands for Calvin–Benson–Bassham cycle, the dominant CO_2 fixation pathway. Circles are numbered to show various microbial taxa and are colored based on their phylogenetic origins: 1 for *Sulfuritalea*- and *Sulfuricella*-like taxa, 2 for *Thiobacillus*- and *Thauera*-like taxa (class β-proteobacteria); 3 for Rhodospirillaceae (class α-proteobacteria); 4 for Ectothiorhodospiraceae, 5 for Methylococcaceae (class γ-proteobacteria); 6 for Brocadiaceae (phylum Planctomycetes); 7 for Desulfobulbaceae and Desulfovibrionaceae (class δ-proteobacteria); 8 for Bacillaceae, 9 for Peptococcaceae including *Candidatus Desulforudis* (phylum Firmicutes); 10 for ANME, 11 for methanogenic Methanosarcinaceae (phylum Euryarchaeota). Orange bars indicate S–N coupling due to the abundant autotrophic, sulfur-oxidizing, denitrifiers *Sulfuritalea*, *Thauera*, *Thiobacillus*, and *Sulfuricella*. Isotopic data (*SI Appendix*, Table S1) are given in rectangles.

SI Appendix, Table S3). In addition to the CBB cycle, multiple CO_2 fixation pathways detected in the metagenome (23) were expressed, namely, reverse tricarboxylic acid cycle (rTCA), 3-hydroxypropionate/4-hydroxybutyrate (3-HP/4-HB) pathway, and Wood-Ljundahl (WL) pathway. The ribulose-1,5-bisphosphate carboxylase/oxygenase (RuBisCo) of the CBB cycle is the most abundant (Fig. 1) and closely related to the abundant α- and β-Proteobacteria (*SI Appendix*, Fig. S1). A complete set of the PEGs and encoded enzymes along the methyl branch of the WL pathway was detected (Fig. 1). These are related to those of δ-proteobacterial sulfate reducers rather than homoacetogenic bacteria or methanogens. Sulfate reducers may fix CO or CO_2 (autotrophy), or run the WL pathway in reverse direction to oxidize acetate (heterotrophy), or do both (mixotrophy). Based on $\Delta^{14}C$ and $\delta^{13}C$ analyses of DIC, CH_4, DOC, and bacterial phospholipid fatty acids (PLFAs) from this same fracture fluid, Simkus et al. (23) concluded that $\delta^{13}C_{VPDB}$ values of −54.8‰ to −64.0‰ for bacterial PLFAs were due to carbon uptake of DIC (−43‰) or of methanogenic CH_4 (−54‰), rather than utilization of the DOC pool. Enzymes involved in heterotrophic pathways, such as Embden–Meyerhof–Parnas glycolysis and gluconeogenesis, and in fermentation occurred at much lower abundances compared with those of autotrophic enzymes (Fig. 1), which is consistent with the isotopic data (Fig. 2).

The low abundance of ^{14}C in the DIC indicates that some portion of the DIC is derived from paleometeoric recharge (23, 35). The very low $\delta^{13}C$ values of DIC and their correlation with the $\delta^{13}C$ values of CH_4 demonstrate that the bulk of the DIC was supplied by oxidation of CH_4 generated by hydrogenotrophic methanogenesis (23). This interpretation is supported by the detection of active methanogens and ANMEs ($1.8\%_{rRNA}$ and $0.08\%_{rp}$) in the present study (Figs. 2 and 3). PEGs and proteins corresponding to tetrahydromethanopterin *S*-methyltransferases (MTR) and methyl coenzyme M reductases (MCR) were both expressed (Fig. 1). Except for one *mtr* PEG related to methanogens, all others are related to ANME-1 and *Candidatus Methanoperedens nitroreducens*, which have been proposed to be autotrophic (36, 37). PEGs related to methane monooxygenase of Methylococcaceae were also detected, but at very low abundance (Fig. 1). The metabolic gene expression profiles indicate that the majority of the active community used the CBB cycle to derive its carbon from DIC, which had been recycled through the active CH_4-cycling community (38).

Microbial Syntrophy. We constructed a map of C1 carbon flow among the various chemolithoautotrophic groups, highlighting three pairs of electron-shuttling systems (Fig. 3). One is between ANME and SRB. ANME-2 produce intracellular S^0 from SO_4^{2-} by an unknown pathway (17). The authors proposed that the produced S^0 then reacts with HS^- outside the cells to form polysulfides, which are taken up by the syntrophic SRB and are disproportionated to SO_4^{2-} and HS^-. The resultant SO_4^{2-} may be reused by ANME-2. More recent studies showed that nanowires are synthesized to enable interspecies electron transfer between ANME-1 and ANME-2 and their associated SRB (18, 19). The other two pairs are between ANME and methanogens, and between SOB and SRB.

Methanogenesis (reactions #31–33) and hydrogenotrophic sulfate reduction (reaction #28) clearly represent the thermodynamic bottlenecks in the studied SLiME. On the contrary, the antagonistic reactions CH_4 and S oxidation, respectively, yield two orders of magnitude more power per mole of reactants (*SI Appendix*, Fig. S3). We propose that the most thermodynamically disadvantaged microorganisms, that is, methanogens and SRB in this case, have

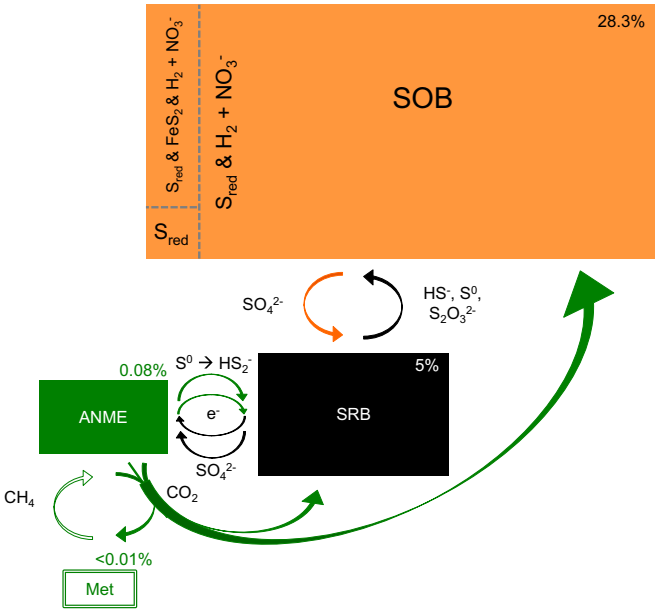

Fig. 3. C1 carbon flow map in the oligotrophic deep subsurface. Microbial groups are represented by rectangles. Rectangle sizes are not scaled to their relative abundances derived from ribosomal proteins in the PEG transcriptome, which are indicated to the top right corners. The color scheme for sulfur oxidizers (SOB), sulfate reducers (SRB), anaerobic methane oxidizers (ANME), and methanogens (Met) is the same as in Fig. 2. Arrows indicate the direction of metabolic transfers between microbial groups and do not imply that direct physical contact is involved. Three electron-shuttling systems occur between the microbial groups, which resulted in three pairs of syntrophic partners. The C in CO_2 is cycled through the syntrophic pair of methanogens and ANME. The CO_2 from anaerobic methane oxidation is being incorporated into the more abundant SRB and SOB. The metabolic versatility of denitrifying SOB to use various electron donors enables them to outnumber their syntrophic partner SRB and become the most dominant chemolithoautotroph in the studied SLiME.

the need to develop a metabolically closely coupled relationship with syntrophic partners. As a result of such partnerships, the thermodynamically difficult reactions, namely, methanogenesis and hydrogenotrophic sulfate reduction, by methanogens and SRB, respectively, can be pulled forward upon the demand of ANME and SOB, respectively. As a result, the fitness of methanogens and SRB should increase. Recycling of metabolic products between syntrophic partners should enable them to maintain their metabolic activities, further resulting in increasing population size over time. Population growth should further strengthen the metabolic exchanges, especially when syntrophic partners are in close physical proximity and/or directly connected (18, 19, 39). This positive relationship between fitness and population size is referred as a positive Allee effect (40, 41). Microbial syntrophy is potentially an influential attribute to a subsurface ecosystem's stability and community dynamics, which has not been previously recognized. Here, we discuss the probable syntrophic interactions in each of the pairs of microbial groups that recycle CH_4 and S.

The millimolar level of methanogenic CH_4 is ample to support growth of ANME and to permit its metabolic independence of ANME from methanogens. However, ANMEs do not thrive but remain as a minority population in the total RNA (*SI Appendix*, Fig. S1), even though CH_4 oxidation by NO_3^- and SO_4^{2-} are among the most thermodynamically highly favored reactions (*SI Appendix*, Fig. S3). Between the two electron acceptors NO_3^- and SO_4^{2-} that are being used by ANMEs, NO_3^- appears to be limiting, whereas SO_4^{2-} is more readily available. To explain the low abundance of ANME, we consider that ANME is syntrophically coupled with methanogens. Although the demand of ANME for CH_4 drives methanogenesis forward and thus maintains the methanogenic population, the ANME's population is indirectly controlled by methanogenic activity of methanogens.

It is less straightforward to deduce the syntrophic partnership between SOB and SRB because reduced S species and SO_4^{2-} may come from nonlocal and/or nonmicrobially mediated processes; consequently, SOB and SRB could live independently. *Thiobacillus denitrificans* is the only species known to obtain S directly from pyrite nanoparticles, but not from large crystals of pyrite (42) such as those found in the Witwatersrand Supergroup (43). The relatively small population of *Thiobacillus* ($3.3\%_{rp}$) is more likely to obtain its S from nanoparticles of pyrite generated by SRB as has been shown to be occurring in anaerobic biofilms of South Africa boreholes that contain both SRB and SOB (44, 45). If the reduced S species came from other mechanisms, for example, as intermediates produced during radiolytic oxidation of pyrite, or from other unidentified sources, then these alternative inputs would have to occur at a rate low enough that no excess HS^- concentration is observed, as evidenced by the low level of measured HS^- (*SI Appendix*, Table S1). The capacity for SOB to couple with SRB therefore has an obvious ecophysiological advantage over foraging the reduced S species from the environment. In exchange, proactive removal of HS^- products from sulfate reduction pulls the reaction in the forward direction.

HS^- produced by SRB may react with Fe(II) ions to form nanoparticle FeS or pyrite and these could either be oxidized by *Thiobacillus*, as discussed, or be radiolytically oxidized to SO_4^{2-}, suggesting that SRB could live independently from SOB in the latter case. S oxidation catalyzed by SOB is, however, more efficient than the chemical process. Hence, the dependence of SRB on SOB for the removal of their HS^- products and the regeneration of SO_4^{2-} should enhance the metabolic conditions for SRB.

Interestingly, the C1 carbon flow map also showed that one member of the syntrophic partners is more abundant than the other (SOB > SRB; SRB > ANME; ANME > methanogens) (Fig. 3). As a matter of fact, the C in CO_2 that has gone through the CO_2–CH_4 cycle by the syntrophic pair of methanogens and ANMEs ("trophic 1") is being incorporated into the more abundant SRB and SOB ("trophic 2"), which emerged as an "inverted biomass pyramid" that is composed of exclusively autotrophs. In a typical food chain (e.g., a large fish feeds on a medium fish, which in turn feeds on a small fish), carbon and energy are derived from the same organic compounds, with less than 10% of the energy being used to generate new biomass and the remaining being dissipated as heat. The consumers are therefore not expected to outnumber the producers or the prey, except during the occurrence of inverted biomass pyramids in oligotrophic lakes due to the fast turnover rate of primary producers, allochthonous DOC inputs, or the presence of refugia (40, 46, 47). On the contrary, as chemoautotrophs derive carbon and energy from different substrates, the CO_2 leaked from the CH_4 cycle becomes available for the greater productivity of SRB and SOB, whereby the carbon fixation process has no direct chemical coupling with the redox reactions. Due to the decoupling of energy and carbon acquisition, differential population sizes between the syntrophic partners and the apparent inverted biomass pyramid would be determined by the relative difference in the amounts of electron donors and acceptors available to various microbial groups. To test this hypothesis, we examined the bioenergetics of SOB and SRB based on the aqueous chemistry of the sample. Population dynamics of SOB and SRB were modeled over a 35-ky period to reproduce the observed geochemistry. All models were constrained by measured growth yields and kinetics of cultivated bacterial strains (*Materials and Methods*).

The model results showed that the autotrophic SRB are consistently less abundant than the SOB (*SI Appendix*, Fig. S4), which is consistent with the metatranscriptomic and metaproteomic results discussed above. Thermodynamic calculations also indicated that the sulfur–oxidation/nitrate–respiration coupling is energetically more productive than hydrogenotrophic sulfate reduction (reaction #28 in *SI Appendix*, Fig. S3). Decreasing the NO_3^- flux reduces the cell concentration of denitrifying SOB to a lower level (*SI Appendix*, Fig. S4 *A* and *B*). In hydrothermal vents, thermodynamic modeling suggested that H_2 and S oxidation contributed 20% and 80%, respectively, of the energy budget in the ubiquitously distributed SOB SUP05 (48). Because SOB *Sulfuritalea hydrogenivorans* has been demonstrated to oxidize H_2 (30), evidence of SOB expressing hydrogenase was sought. Among the hydrogenase-encoding transcripts detected, about 47% are related to *Sulfuritalea hydrogenivorans*. Metabolic versatility could thus contribute to the dominance of SOB in the studied system.

The addition of H_2 oxidation reactions to the thermodynamic models of SOB and SRB, however, caused the SRB population to decline (*SI Appendix*, Fig. S5), likely due to competition for H_2. This prediction implies that the SRB could have been outcompeted and eventually eliminated from the community, which did not happen, as indicated by the detection of SRB and their expression of sulfate-reducing genes and enzymes. Although the underlying mechanism that has prevented SRB from elimination by H_2 competition is not clear at this moment; possible explanations are discussed here. As some portions of hydrogenases and sulfur-oxidizing enzymes were coexpressed within SOB denitrifiers, their intracellular regulatory systems would control in part the amount and rate of H_2 being taken from the environment. Recently, the aerobic SOB *Thiomicrospira* sp. strain SP-41 isolated from low-temperature hydrothermal fluids showed that co-oxidation of millimolar $S_2O_3^{2-}$ and micromolar H_2 yielded 10 times more cells than the micromolar H_2-only experiment did, although the H_2 consumption rate was four times lower in the $S_2O_3^{2-}$/H_2 experiment (49). However, no empirical data on the relative contribution of H_2 and S oxidation to the energy budget in SOB denitrifiers are available to constrain the model, which currently treated H_2 and S oxidation coupled to NO_3^- reduction as two independent reactions. As the H_2 consumption rates by aerobic SOB vary under different conditions, the idea of H_2 uptake by SOB denitrifiers being a negative feedback in this syntrophic relationship is plausible but it needs to be tested. Another possibility is that H_2-utilizing microorganisms may be spatially separated (on a not-yet-known scale) to reduce the competition, which then suggests that the H_2-oxidizing SOB individuals may be physically distant from SRB. Additional experiments will be required to resolve the factors influencing syntrophy and competition (or the "love-and-hate relationship") between these SOB and SRB.

Under the oligotrophic conditions that SLiMEs occur, their community structure will likely change in response to changes in

nutrient availability and environmental conditions. Consequently, the relative abundance of the syntrophic partners may shift and the apparent inverted biomass pyramid may become upright. The spatial and temporal scales over which syntrophic SLiMEs migrate and evolve require further investigation because these two processes ultimately control the distribution of SLiMEs in the deep subsurface.

Concluding Remark

The approach described in this study provides a comprehensive portrait of the active metabolic landscape of a SLiME enabled by syntrophic metabolic interactions. The fluxes of energy sources and the capability of using multiple electron donors explain the occurrence of an apparent inverted biomass pyramid of chemolithoautotrophs at the deep subsurface. Unlike previously described deep subsurface ecosystems, H_2-driven autotrophic processes (sulfate reduction, methanogenesis, and subsequent anaerobic CH_4 oxidation) are not the dominant metabolisms but instead support the predominant sulfur-driven denitrification. The metabolic capability of the predominant sulfur-driven autotrophic denitrifiers drives the links between the N, S, and C cycles. Previous studies have reported the high energetic potential of S–N reactions in other deep continental sites (50), and expression of mRNA coding for nitrate reductase in marine subseafloor sediment cores where NO_3^- was not detectable (51), indicating that the role of nitrate reduction and/or denitrification in the deep subsurface has been overlooked. Active subsurface metabolic landscapes that intertwine H_2-driven processes, S–N coupling, and dissimilatory NO_3-dependent reactions may be more prevalent in both continental and marine subsurface systems than previously thought. This study expands the range of metabolic landscapes, which should be considered when exploring the potential of extinct and extant life elsewhere in the solar system on terrestrial planets and moons.

Materials and Methods

Microbial Biomass Collection. The RNA and protein samples used in this study were coextracted with DNA from the filter, BE326FW270712 Bh2. The detailed description of the study site (BE326 BH2), sample collection, and extraction protocol of this sample has been published in Lau et al. (21) and Magnabosco et al. (8). Briefly, fracture fluid at 1.34 km below land surface was filtered onsite at Beatrix gold mine shaft no. 3, level 26, which is situated at southwest of the 2.9-Ga Witwatersrand Basin (quartzite and shale), using a sterile stainless-steel manifold that was installed onto the stainless-steel borehole casing. Approximately 86,400 L of water was filtered over 15 d, at an initial water flow rate set at 4 $L{\cdot}min^{-1}$. Biomass captured on the preautoclaved Memtrex NY filter (MNY-91-1-AAS; pore size of 0.1 μm; General Electric) was preserved in RNA-preservation solution [20 mM EDTA, 0.3 M sodium citrate, and 4.3 M ammonium sulfate; pH adjusted to 5.2 using concentrated H_2SO_4 (21)] and stored at −20 °C until extraction.

RNA and Protein Extraction. Total RNA and protein, together with total DNA, were extracted using 2× CTAB lysis buffer and phenol/chloroform (pH 6.5–6.9). Total RNA was resuspended in 1× TE-buffer (Tris-EDTA, pH 8) and stored in 1.5-mL Eppendorf tubes at −20 °C (21). To reduce RNA degradation during the extraction process, all extraction tubes were kept on ice between steps. An aliquot of the nucleic acid sample was treated with DNase I (catalog #AMPD1; Sigma-Aldrich) following the manufacturer's instructions, which included a 15-min incubation at room temperature and an inactivation step at 70 °C for 10 min. PCR amplification of the treated RNA yielded no PCR products after 35 cycles, indicating the sample was DNA-free.

Total protein was purified from the organic fraction by standard methanol/acetone purification. In brief, debris at the interface layer was removed before adding five volumes of chilled methanol and ammonium acetate (100 mM final concentration). The mixture was incubated overnight at −20 °C. Protein was pelleted at 17,000 × *g* for 20 min with supernatant discarded afterward. Protein pellets were washed with chilled HPLC-grade methanol and collected by centrifugation at 17,000 × *g* for 10 min. Methanol was discarded. The wash step finished with two additional rounds of HPLC-grade acetone. The protein pellets were air-dried for 5–10 min and stored in 1.5-mL Eppendorf tubes at −20 °C.

Directional RNA-Sequencing. Before sequencing, the total RNA sample was analyzed on the Agilent 2100 BioAnalyzer system using RNA 6000 Nano kit. The size distribution plot showed that the sample quality was good for RNA sequencing for the following reasons: fragments as long as ∼3,000 bp (the size of intact large subunit of rRNA gene) were present, fragment intensity peaked at size of ∼750 bp, and a visible, discrete peak at ∼1,500 bp, which is indicative of intact small subunit of rRNA genes. The high-quality RNA was treated using RNase III (0.5 mM final concentration) and resulted in a majority of 500-bp-long fragments. The RNA products from the controlled fragmentation step were used to prepare the strand-specific metatranscriptomic library, following the manufacturer's instruction of Apollo 324 PrepX mRNA library protocol (IntegenX), which is based on directional RNA adaptor ligation. Library concentration was quantified on Agilent 2100 BioAnalyzer DNA HS chip using Qubit DNA HS assay (Life Technologies). The library of this sample was pooled in equal molar ratio with three others. Absolute quantitative PCR assay using SYBR FAST ABI Prism QPCR Mast Mix (Kapa Bio Systems) was performed to confirm amplification efficiency and to determine the library loading concentration for sequencing. Sequencing of 141-nt single-end reads was performed on one lane of Illumina 2500 HiSeq platform with Illumina's Truseq Rapid SBS chemistry. This protocol generated sequences that are in the same orientation as the actual transcripts.

Quality Control of RNA-Seq Data. A total of 29,980,240 single-end reads were generated from total RNA. The fastq data were filtered for high-quality reads using the tools on https://galaxy.princeton.edu. The quality control (QC) was run in the following order: (*i*) removed reads that contain 90% of bases with Phred quality score (Q score) lower than 30 (i.e., error probability of base calling, 0.001); (*ii*) screened for reads that matched the first 30 bp of the 3′-end adapter sequence (5′-AGATCGGAAGAGCACACGTCTGAACTCCAG-3′) anywhere along the read length, with search criteria set to maximum error rate of 0.1, match times of 1, minimum overlap length of 20, allow "Ns" in the read over aligned region as matches, then clipped off the portion following the adapter sequence; (*iii*) clip from the 3′-end of the reads that matched with the above 30-bp adaptor sequence and discard reads that contained Ns and that were shorter than 50 nt. The QC-run resulted in 21,577,391 reads (average read length of 123 ± 21 nt) that had an average Q score higher than 30 at each nucleotide position.

De Novo Metatranscriptome Assembly. The high-quality RNA reads were organized into two subsets, protein-coding RNA (cRNA) sequences and noncoding RNA (ncRNA) sequences. First, all high-quality RNA reads were searched against four databases using USEARCH (52). The four databases (DBs) were transfer RNA DB (53, 54) (872,667 sequences), 5S rRNA DB (55) (last updated in September 2005; 1,379 sequences), small and large rRNA DBs (56) (version 119.1; 4,346,329 sequences in SSUParc_tax_silva.fasta.gz and 446,998 sequences in LSUParc_tax_silva.fasta.gz). Then, RNA reads were assigned into the ncRNA subset when they shared at least 80% of identity in global alignment with any of references in the four DBs, regardless of the orientation. The options used were "–usearch_global," "–uid 0.8," "–strand both," and "–threads" for multithreading. The remaining RNA reads were assigned into the cRNA subset. RNA reads were parsed into cRNA and ncRNA subsets, containing 1,498,563 (7%) and 20,078,828 (93%) reads, respectively, by a Python script.

The cRNA and ncRNA subsets were assembled separately using de Bruijn graph-based de novo transcriptomic assemblers. The "strand-specific" option was indicated in the execution commands. Transcript contigs in the final assemblies have minimum length of 200 nt. The cRNA subset was assembled using Trinity (57), version r20131110, with the default settings, whereas the ncRNA subset was assembled using Trans-ABySS (58) (version 1.5.2). To run Trans-ABySS, contigs were first constructed from 61 to 101 *k*-mers, with an incremental step of 4 mers, as separate assemblies using ABySS (version 1.5.2) (59). These assemblies were then merged by Trans-ABySS.

Annotation of Transcript Contigs. Transcript contigs were clustered using the CD-HIT package, version 4.6.4 (60). The mRNA transcript contigs generated from the cRNA assembly were first subjected to gene prediction. Prodigal, version 2.6.1 (61), was used to identify open reading frames using the option "–p" for metagenome and translation table 11. Because the orientation of our RNA-seq reads was known and all of the transcript contigs ran in the sense direction, any predictions made for the antisense orientation were discarded. A Python script was used to extract the amino acid sequences translated from the sense strands. The protein-encoding genes (PEGs) generated from the mRNA transcript contigs were clustered using the CD-HIT algorithm. Peptides were clustered at 90% of identity (word size, "–n" = 5) in local alignment ("–G" = 0), using a slow mode ("–g" = 1) such that the query sequence would be clustered into the most similar cluster that meet the threshold of 80% of the shorter sequence was aligned ("–aS" = 0.8). The longest sequence in each cluster was searched against the National Center for Biotechnology Information (NCBI) nonredundant protein (nr) database for the best ten hits using BLASTp. Using a Python script, the 10 hits were first evaluated based on an alignment of >50% of the query sequence, an e-value <1e-5, and a bit score >50, and then the query sequence was assigned with the consensus protein identity by majority rule based on the description of each NCBI entry. Representative sequences that

resulted in no and low-confident BLASTp hits, and all mRNA transcript contigs in the represented clusters, were omitted from further analysis. Phylogenetic origins of these PEG transcripts were inferred from the BLASTp hits that passed the quality thresholds as a means to validate that the microorganisms expressing the metabolic functions generally matched with what would be expected from the PEG transcriptome of ribosomal proteins and the rRNA transcriptome. However, expression levels of rRNA and ribosomal protein transcripts were the preferred choice for showing taxonomic abundances and were presented in the paper.

Transcript contigs of ncRNA, primarily rRNA genes, were clustered using the CD-HIT-EST algorithm at an identity cutoff level of 95% (word size, "–n" = 10). The longest sequence in each cluster was searched against the rRNA database that comprised of SILVA SSU and LSU sequences (version 119) for the best 10 hits using BLASTn. Using a Python script, the 10 hits were first evaluated based on an alignment of >50% of the query sequence, an e-value <1e-5, and a bit score >50, and then the query sequence was assigned with the consensus rRNA identity by majority rule, and taxonomic rankings were assigned by the lowest common ancestor (LCA) principle (threshold = 80%). The same rRNA database was used to identify chimeric rRNA gene sequences using UCHIME (62). The rRNA transcript contigs in clusters that were represented by a chimeric sequence were omitted from further analysis. Also, representative sequences that resulted in no and low-confident BLASTn hits, and all rRNA transcript contigs in the represented clusters, were omitted from further analysis.

Abundance of Transcript Contigs. The cRNA and ncRNA datasets were mapped to the cRNA and ncRNA assemblies, respectively using Bowtie 2, version 2.2.5 (63), options "–end-to-end" for global alignment, "–norc" for known strand specificity, and "–very-sensitive" mode for higher accuracy. Coverage was calculated for each contig by normalizing the number of reads mapped to the contig to its length:

$$\frac{\text{Number of mapped reads} \times \text{Average read length (nt)}}{\text{Contig length (nt)}}.$$

Abundance of each PEG cluster and each consensus protein was computed by summing the coverage of constituent mRNA transcript contigs. Relative abundance was calculated with respect to the total coverage of mRNA transcript contigs that met the quality criteria. For PEG clusters identified as ribosomal proteins, the taxonomic classifications of the best BLASTp hit were assigned to the cluster as one of the proxies to describe the taxonomic diversity in the studied sample. Similar to the PEG transcriptome, abundance of each rRNA cluster was computed by summing the coverage of constituent rRNA transcript contigs. Relative abundance was calculated with respect to the total coverage of rRNA transcript contigs that met the quality criteria.

Relative Abundance within Rhodocyclaceae. Because the rRNA transcriptome and the mRNA transcriptome of ribosomal proteins showed different genera composition structure within the most dominant β-proteobacterial family Rhodocyclaceae, a reciprocal best-hit BLAST search was performed using the representative PEGs of the CD-HIT clusters to provide an additional, independent view. Reciprocal best-hits BLAST approach is a more restrictive annotation method commonly used in comparative genomic analyses. As of November 29, 2015, 21 genomes of Rhodocyclaceae were published on NCBI and the PEG sequences were downloaded. The PEGs in our PEG transcriptome and the Rhocyclaceae PEGs were compiled separately into two searchable databases using the "makeblastdb" tool in the ncbi-blast-2.2.29+ package (64). The representative PEG sequences and Rhocyclaceae amino acid sequences were then searched reciprocally to obtain the best BLASTp hit using the option "–max_target_seqs 1." The best hits with an e-value <1e-5 and a bit score >50 were considered valid. The representative PEG sequences that formed pairs of best hits with Rhodocyclaceae genome PEGs in both searches were considered to be Rhodocyclaceae and were assigned with a functional and a taxonomic identity. Relative abundance of Rhodocyclaceae PEGs identified in our PEG transcriptome was calculated as mentioned above.

UltraHigh-Performance Liquid Chromatography–Tandem Mass Spectrometry Analysis. Total protein pellet, extracted as mentioned above, was dissolved in hot 7 M urea/2 M thiourea/100 mM Tris solution (pH 8.0), which was subjected to thiol reduction alkylation using DTT and iodoacetamide, followed by in-solution trypsin proteolysis using the FASP procedure (65). The digested peptides were fractionated into 10 fractions by strong cation exchange chromatography using a Dionex Ultimate NanoLC capillary HPLC system (Dionex) using a gradient from a 75%/25% (vol/vol) mix of buffers A:B to 100% buffer B (buffer A: 7 mM KH_2PO_4, pH 2.65, 30% (vol/vol) acetonitrile; buffer B: 7 mM KH_2PO_4, 350 mM KCl, pH 2.65, 30% (vol/vol) acetonitrile). Each of these fractions was analyzed by high-resolution nano–ultrahigh-performance liquid chromatography (UPLC)-tandem mass spectrometry (MS/MS) analysis on an accurate-mass linear trap quadropole (LTQ) OrbiTrap Elite platform (Thermo Fisher Scientific), outfitted with an Easy nLC 1000 UPLC system (Thermo Fisher Scientific) and a Flex ion source (Thermo Fisher Scientific). Separations were performed using a trapping capillary column (150 μm × ∼40 mm, packed with 3 μm, 100 Å Magic AQ C18 resin; Michrom) at a flow rate of 4 $\mu L \cdot min^{-1}$ for 4 min, followed by an analytical capillary column (75 μm × ∼50 cm, packed with 3-μm, 100-Å Magic AQ C18 resin; Michrom) under a linear gradient of A and B solutions (solution A: 3% acetonitrile/0.1% formic acid (vol/vol); solution B: 97% acetonitrile/0.1% formic acid) from 5–35% (vol/vol) B over 180 min at a flow rate of 300 $nL \cdot min^{-1}$. Nanospray was achieved using commercial sprayer tips (New Objective) at a voltage of 2.4 kV, with the Elite heated capillary at 275 °C. Full-scan (*m/z* 335–1,800) positive-ion mass spectra were acquired in the LTQ Orbitrap at a resolution setting of 120,000. MS/MS spectra were simultaneously acquired using collision-induced dissociation method (CID) in the LTQ OrbiTrap for the top 20 most abundant multiply charged species in the full-scan spectrum having signal intensities of >1000 NL. Lock mass was used, maintaining calibration to 2–3 ppm of accurate mass. All samples were analyzed in technical duplicates.

Protein Identification from UPLC-MS/MS Data. MS/MS data were analyzed in aggregate using the SEQUEST HT search engine in ProteomeDiscoverer, version 1.4 (Thermo Fisher Scientific), to search against a sample-specific metaproteome database (66), which was created by compiling the in silico translation of the PEG sequences. Search parameters included trypsin digestion with up to one missed cleavage, methionine oxidation, and cysteine carbamidomethylation. A peptide-level false-discovery rate of 5% was achieved by using the Percolator node in ProteomeDiscoverer, which uses the frequency of matching against a decoy database as a rigorous model of the probability of error in the forward matches at given score thresholds. Numbers of peptide-spectral match (PSM) were used as a surrogate measure of protein abundance.

A PEG was considered positively validated as an expressed protein if one of the following criteria were met: (*i*) the PEG was identified by matches to two unique peptides in replicated UPLC-MS/MS runs; (*ii*) if it was identified only in one run, but at least two unique peptides in the PEG were matched; or (*iii*) if it was identified only in one run and by a single unique peptide, but at least five PSMs were assigned to the PEG.

Geochemical Sample Collection and Analyses. Procedures for the collection and preservation of dissolved gas and aqueous species of the fracture fluid followed established protocols for underground sampling. Filtered water samples for anion and cation measurements were collected following the methods described in Moser et al. (67). Fracture water was filtered through Whatman polycap 36 TC filter (which was later used for RT-PCR cloning; *SI Appendix, SI Materials and Methods*) into 50-mL Nalgene bottles. Dissolved cation samples were preserved with 200 μL of concentrated HNO_3. A gas stripper was connected to the manifold for gas sampling. Dissolved gases were then transferred into preevacuated 160-mL vials using a 50-mL gas-tight syringe following the procedure described in Ward et al. (68). Noble gas samples were collected according to Lippmann et al. (25), the 20-mL copper sampling tube was flushed with sample water, and while water was flowing, the copper tube was sealed by crimping it with stainless-steel clamps on the effluent end and then the influent end.

For sulfur isotopic analyses, fracture fluid was filtered through a 0.2-μm filter paper and collected in a 1-L Nalgene bottle. HS^- in the water was fixed as CdS by preadded excess amount of $CdCl_2$ in the sample bottle. The water sample was then stored and shipped to the laboratory while cold and stored cold for the following further processing. HS^- was extracted from the CdS residues collected after filtration. SO_4^{2-} was extracted subsequently by adding an excess amount of $BaCl_2$ into the filtered water followed by filtration of $BaSO_4$ precipitates. Both CdS and $BaSO_4$ were converted into Ag_2S, which was then dried and put into a nickel bomb to react with F_2. The SF_6 product was finally released from the nickel bomb, purified, and sent to an isotope-ratio mass spectrometer for sulfur isotope analysis. All data are reported relative to the Vienna Cañon Diablo troilite (VCDT) standard. Analytical precision for $\delta^{34}S$ is 0.2‰ (2σ).

For stable isotopic analysis of N_2, gas samples collected in July 2011 were first characterized by a mass spectrometer coupled with gas chromatography for concentrations of all major gas components (hydrocarbons, CO_2, noble gases, H_2, O_2, and N_2). Only the samples with little or no air contamination were used for subsequent N isotope analysis. The gas samples were injected into a gas chromatographic to separate then carried in a helium continuous flow stream to an isotope ratio mass spectrometer (Thermo Finnigan DeltaPlus) for N isotope measurements. The $\delta^{15}N$ values were reported relative to the Air standard, and analytical precision was 0.2‰ (2σ).

For stable isotopic analysis of NO_3^-, fracture fluid was filtered through a 0.2-μm filter paper and collected in a 100-mL Nalgene bottle that was previously

rinsed with 10% (vol/vol) HCl and MilliQ water. The water sample was kept in a cooler of reusable ice packs immediately upon reaching the surface and during transport, and stored at −20 °C until processing. The $\delta^{15}N$ and $\delta^{18}O$ of NO_3^- were measured by the "denitrifier method" (69, 70), wherein a denitrifying bacterial strain lacking nitrous-oxide reductase quantitatively converts sample NO_3^- and NO_2^- to N_2O. The isotopic composition of N_2O was measured by GC-IRMS using a Thermo MAT253 mass spectrometer (Thermo Finnigan DeltaPlus) and a purpose-built on-line N_2O extraction and purification system. The international reference materials, IAEA-N3 and USGS-34, were used for calibration to the air N_2 and Vienna standard mean ocean water (VSMOW) scales. An in-house N_2O standard was run in parallel to monitor mass spectrometry. Analytical precision for the system used has been characterized as ≤0.1‰ for $\delta^{15}N$ and ≤0.2‰ for $\delta^{18}O$ (2σ) for the NO_3^- concentration analyzed here. Because NO_2^- is included in the isotopic analysis (70), before isotopic analysis, NO_2^- was removed by a sulfamic acid protocol described in Granger and Sigman (71). Measurements were made in three technical replicates. Due to an unidentified problem of N_2O conversion in the 2012 sample, isotopic values of NO_2^--removed sample collected in 2011 were reported.

The concentrations of the atmospheric noble gas isotopes (72) (^{36}Ar, ^{84}Kr, ^{86}Kr, and ^{129}Xe) are a fraction of those for groundwater in equilibrium with the atmosphere at the mean annual temperature for central South Africa. This indicates that the fracture water has lost some of its dissolved gas, presumably to the head space of the fractures during dewatering of the fractures by the mining operations. We used the diffusion model of Lippmann et al. (25) and the concentrations of ^{36}Ar, ^{84}Kr, ^{86}Kr, and ^{129}Xe to correct the concentrations of all of the noble gases as well as the concentrations of dissolved gases, H_2, O_2, N_2, N_2O, CH_4, CO, NH_3, and H_2S. The diffusion coefficients compiled by Cussler (73) was used, and for the diffusion coefficient of N_2O the experimental data of Tamimi et al. (74) was used.

Calculation of Subsurface Residence Times. The subsurface residence times for the bulk water were calculated from the diffusion-corrected concentrations of ^{40}Ar, ^{134}Xe, and ^{136}Xe [determined by Purtschert et al. (72)] using the flux model equations and parameters of Lippmann et al. (25). The age estimates range from 3 to 14 my, consistent with previous analyses of subsurface fracture water reported by Lippmann et al. (25).

Calculation of Free Energy Fluxes. Steady-state free energy fluxes of 37 energy-yielding redox reactions for autotrophy, heterotrophy, methanotrophy, and methanogenesis were estimated as described in Onstott (75) and Magnabosco et al. (4). The Gibbs free energy of each reaction was calculated using the measured cation, anion, and dissolved gas concentrations (*SI Appendix*, Table S1) and The Geochemist's Workbench (GWB), version 8.0 (76) (Rockware). The free energy flux was calculated using the following equation from Onstott (75):

$$\text{Free Energy Flux } \left(\text{kJ}\cdot\text{cell}^{-1}\cdot\text{s}^{-1}\right) = 4\pi rDC\Delta G, \quad [1]$$

where r is the average radius of a cell (in centimeters) and assumed to be 7.5×10^{-5} cm, D is the diffusion constant (in square centimeters per second) of the limiting reactant corrected for the in situ temperature, C is the concentration of the limiting reactant (in moles per cubic centimeter), and ΔG is the in situ Gibbs free energy per mole of the limiting reactant (in kilojoules per mole).

This expression assumes that the measured concentrations represent a steady-state dynamic equilibrium of a planktonic microorganism.

For microbial redox reactions that involve sessile microorganisms that are bound to a mineral surface and are using a mineral phase [for example, FeS_2, $Fe(OH)_3$, and pyrolusite] as electron acceptor, the effective diffusion constant (D_{eff}) of the electron donor was adjusted according to the following equation:

$$D_{\text{eff}} = D\frac{\phi\cdot\delta}{\tau^2}, \quad [2]$$

where ϕ is porosity of the hard mineral phase, δ is constrictivity, and τ is tortuosity. For the purpose of this study, the porosity of the Witwatersrand Basin rock units was assumed to be 0.005 (29), $\delta = 1$, and $\tau = 3$ (77).

For the reactions containing gaseous species, the Gibbs free energy and the free energy flux were calculated for both the measured concentrations and for the diffusion-corrected gas concentrations. The difference in the Gibbs free energy for the measured concentrations and the diffusion-corrected gas concentrations was the greatest for those reactions using H_2 and NH_3. H_2 has the highest diffusion rate of all gas species and as a result will be the most readily depleted in a fracture where head space is present. Because the pH is elevated, NH_3 is more abundant than NH_4^+ and will also preferentially partition into any head space. For example, the Gibbs free energy for the reactions for autotrophic acetogenesis and methanogenesis by CO_2 reduction (#34 and #32 in *SI Appendix*, Fig. S3, respectively) were both slightly positive for the measured concentrations, but were slightly negative for the diffusion-corrected gas concentrations. The only microbial reaction impacted by the loss of NH_3 to the head space is the ANAMMOX reaction (#10 in *SI Appendix*, Fig. S3).

Biogeochemical Model. GWB was used to model the mixing between an ancient, saline end member and young, low-salinity, recharge water, the radiolytic generation of H_2, O_2, and H_2O_2 and microbial chemolithotrophic reactions. The chemistry for the saline end member of the Witwatersrand Supergroup was derived from the average of fluid inclusion extracts (29) and the young, low-salinity, recharge water was derived from the average ground water analyses published by Abiye et al. (78). The rate of mixing of the pore water in the Witwatersrand quartzite with the meteoric recharge water until the composition of the borehole BE326 Bh2 water chemistry was attained was assumed to be ∼1 My based upon the noble gas data. Given that the Cl^- and NO_3^- concentrations in the saline end member are 1.5 M and 6 mM, respectively, and the Cl^- concentration of the borehole BE326 Bh2 water is 65 mM, the NO_3^- concentration of the borehole BE326 Bh2 water derived from simple mixing would be 300 μM. If this mixing occurred uniformly over the 1 My of groundwater migration, then the mixing rate for NO_3^- would be ∼0.3 $\text{nM}\cdot\text{y}^{-1}$.

The radiolytic production rates, based upon the average U, Th, and K content of the Witwatersrand quartzite and measured porosities (29), are 0.4 $\text{nM}\cdot\text{y}^{-1}$ for H_2 and 0.2 $\text{nM}\cdot\text{y}^{-1}$ for O_2. The production rate of H_2O_2 was 0.05 $\text{nM}\cdot\text{y}^{-1}$, and it was assumed that this H_2O_2 reacted immediately with pyrite to generate sulfate. Based upon the stoichiometry of the reaction, $FeS_2 + 7.5\ H_2O_2 \rightarrow 5.5H_2O + 0.5Fe_2O_3 + 4H^+ + 2SO_4^{2-}$, this rate of H_2O_2 production is equivalent to a SO_4^{2-} production rate of ∼0.02 $\text{nM}\cdot\text{y}^{-1}$. These fluxes for O_2, H_2, SO_4^{2-}, NO_3^-, and NH_4^+ were used to sustain chemolithotrophic microbial reactions.

The microbial respiration rates for methanogenesis, SO_4^{-2} reduction, HS^- oxidation, and H_2 oxidation were based upon published laboratory culture experiments that provided minimum free energy estimates or threshold concentrations (ΔG), kinetic rate constants, such as V_{max}, and the half-saturation Michaelis–Menten constants, K_{m}, and growth yields when available. The following expression was used for calculating the microbial respiration rate of planktonic microorganisms in the fracture water:

$$k = V_{\text{max}}\cdot[X]\cdot F_D\cdot F_A\cdot F_T, \quad [3]$$

where the reaction rate, k, is in moles·(kilogram of water)$^{-1}$·second^{-1}, V_{max} is the intrinsic rate constant of the electron donating and accepting reactions in moles·(milligram of biomass)$^{-1}$·second^{-1}, $[X]$ is the concentration of cells in milligrams of biomass·(kilogram of water)$^{-1}$ (79, 80). F_D is the parameter controlling the electron-donating reaction and is defined by Eq. **4**, and the electron-accepting reaction, which is controlled by the parameter, F_A, is defined by Eq. **5**:

$$F_D = m_D/(m_D + K_D), \quad [4]$$

$$F_A = m_A/(m_A + K_A), \quad [5]$$

where m_D is the electron donor concentration, m_A is the electron acceptor concentration, and K_D and K_A are Michaelis-Menten constants in units of molar. The thermodynamic potential factor, F_T, is defined as follows:

$$F_T = 1 - e^{-f/(xRT)}, \quad [6]$$

where R is the universal gas constant 8.314 $\text{J}\cdot\text{K}^{-1}\cdot\text{mol}^{-1}$, T is the temperature in Kelvin, x is the average stoichiometric number (81), or the ratio of the free energy change of the overall reaction to the sum of the free energy changes for each elementary step, and f is the net thermodynamic driving force of the reaction defined by the following:

$$f = -\Delta G - m\cdot\Delta G_p, \quad [7]$$

where ΔG is the free energy change of the redox reaction, m is the number of moles of ATP generated per mole of reactant, and ΔG_p is the free energy for the phosphorylation reaction (82). The ΔG_p for the phosphorylation reaction, ADP + P → ATP, can vary from about 40–70 kJ·(mol of ATP)$^{-1}$ depending upon the temperature, pH, and concentrations of ADP and ATP in the cell (83, 84) and ranges from 50 to 88 kJ·(mol of ATP)$^{-1}$ if a thermodynamic efficiency of 80% is assumed. However, the $m\cdot\Delta G_p$ was assumed to be 60 kJ·(mol of ATP)$^{-1}$ except in the case of H_2 oxidation reactions for which experimental data were used to constrain the threshold energy. The parameters used in GWB simulation are listed in *SI Appendix*, Table S7.

Simulations were then run incorporating microbial growth and maintenance energy demand rates to determine a microbial community composition based upon the reactant fluxes and microbial respiration rates calculated from the above Eqs. **3**–**7**. The sustainable cellular concentrations within the fracture water were calculated in the GWB by assuming that the growth rate will be proportional to the relative magnitude in the difference between the maintenance energy demand and the rate of energy delivery of a metabolic redox equation defined as ΔP:

$$\Delta P = -0.8\Delta G_r k - m_E \cdot \frac{g_c}{3{,}600}, \quad [8]$$

where ΔP is in kilojoules·(milligram of biomass)$^{-1}$·second^{-1}, ΔG_r is the free energy of the metabolic redox reaction at in situ temperature, activities, and fugacities, which is usually negative, in kilojoules·(mole of reactant)$^{-1}$, k is the metabolic redox reaction rate in moles of reactant·(milligram of biomass)$^{-1}$·second^{-1}, g_c equals to 4.2×10^{-5} moles of carbon per 1-mg dry weight of cell, and m_E is the maintenance energy demand in kilojoules·(mole of C biomass)$^{-1}$·hour^{-1}. k is dependent upon ΔG_r such that when the ΔG_r becomes less negative than a threshold energy, then k will be zero. We also assume that only 80% of the free energy is available for metabolism and the rest is lost as heat. m_E is defined by the following equation from Tijhuis et al. (85):

$$m_E = 4.5 \cdot e^{\left[-69{,}400 \Big/ R\left(\frac{1}{T} - \frac{1}{298}\right)\right]}, \quad [9]$$

where R is the universal gas constant 8.314 J·K^{-1}·mol^{-1}, and T is temperature in Kelvin. The rate of increase or decrease of the biomass is governed by the fraction of the ΔG_r that is directed to maintenance and the growth yield, so the biomass, [X], increases according to the following relationship:

$$[X]_i = [X]_{i-1} + \frac{Y \cdot [X]_{i-1} \cdot \Delta P}{-\Delta G_r}, \quad [10]$$

where $[X]_i$ is the biomass concentration in milligrams of biomass·(kilogram of water)$^{-1}$ at time step i, and Y is the growth yield in milligrams of biomass·(mole of reactant)$^{-1}$.

The m_E relationship is based upon chemostat experimental data across a range of temperatures and is consistent with aerobic and anaerobic microorganisms having similar maintenance requirements dependent only upon the ambient temperature. For simplicity, we make the same assumption in our model. Onstott et al. (86) and Hoehler and Jørgensen (87) point out that the maintenance energy values from Eq. **9** appear to be two to three orders of magnitude greater than retentostat measurement of the maintenance energy rate (88), but to match the observed cellular abundance calculated from our model with the observed cellular concentration we only had to decrease the preexponential term from 4.5 to 4.5×10^{-1}. The addition of the maintenance energy rate to the GWB microbial kinetic function using a custom rate law enabled stabilization of the biomass as the concentrations of reactants and products change during the course of reaction progress and more accurately simulates subsurface populations existing in oligotrophic environments.

The growth yields for HS^- oxidation by O_2 and NO_3^- reduction were based on experimental observations of $S_2O_3^{2-}$ oxidation by *Thiobacillus* species (89–91) (*SI Appendix*, Table S7). The growth yields, kinetic parameters, and threshold values for the H_2 oxidation by O_2 reduction, and H_2 oxidation coupled to denitrification were derived using GWB based on the experiments performed on *Thiobacillus plumbophilus* (92) and *Parococcus denitrificans* (93, 94), respectively (*SI Appendix*, Table S7).

The growth kinetics for autotrophic sulfate reducers are derived from Kristjansson et al. (95) and Sonne-Hansen et al. (96). The growth yields for autotrophic sulfate reducers are more difficult to constrain. In coculture experiments where acetogenic *Acetobacterium* growing on H_2 and CO_2 was supplying acetate to *Desulfovibrio*, the *Acetobacterium* comprised only 5% of the mixed culture (97). The doubling times for *Desulfovibrio* are twice as long when grown autotrophically as when grown on acetate (97). As a growth yield of 4.8 g·(mol of reactant)$^{-1}$ has been published for *Desulfobacter postgatei* by Widdel and Pfennig (98), we have used a growth yield of 2.4 g·(mol of reactant)$^{-1}$ for autotrophic growth of an sulfate reducer (*SI Appendix*, Table S7).

ACKNOWLEDGMENTS. We are grateful for the support of Sibanye Gold Limited and the management and staff of Beatrix gold mine. We give credit to S. Maphanga (Beatrix gold mine) and other researchers who participated in the field campaigns during July 2012, including Sarah Hendrickson, Michael Pullin, and Kenna Wilkie. We express our appreciation to Moutusi Royand and Genming Luo for assisting with sulfur isotopic analysis, and Sandi M. Smart and Daniel M. Sigman for assisting with nitrate isotopic analysis. We thank Matthew Cahn (Department of Molecular Biology, Princeton University) and the staff of Research Computing (Office of Information Technology, Princeton University), especially Robert Knight, for their technical support with the computational analyses. We greatly appreciate Simon Levin, Henry Horn, and Ken Haste Andersen (Department of Ecology and Evolutionary Biology, Princeton University), and the anonymous reviewers for their constructive comments on the manuscript, especially the interpretation of the inverted biomass pyramids. This work was supported by funding from National Science Foundation [Grants EAR-0948659 and DEB-1441646 (to T.C.O.) and DGE-1148900 (to C.M.)], the Deep Carbon Observatory (Alfred P. Sloan Foundation) [Sloan 2013-10-03, subaward 48045 (to M.C.Y.L.)], and the Center for Dark Energy Biosphere Investigations (C.M.). Partial support for isotopic analyses was provided by the Natural Sciences and Engineering Research Council of Canada (B.S.L.). This article is Center for Dark Energy Biosphere Investigations Contribution 340.

1. Stevens TO, McKinley JP (1995) Lithoautotrophic microbial ecosystems in deep basalt aquifers. *Science* 270:450–454.
2. Moser DP, et al. (2005) *Desulfotomaculum* and *Methanobacterium* spp. dominate a 4- to 5-kilometer-deep fault. *Appl Environ Microbiol* 71(12):8773–8783.
3. Lin L-H, et al. (2006) Long-term sustainability of a high-energy, low-diversity crustal biome. *Science* 314(5798):479–482.
4. Magnabosco C, et al. (2016) A metagenomic window into carbon metabolism at 3 km depth in Precambrian continental crust. *ISME J* 10(3):730–741.
5. Lever MA, et al. (2013) Evidence for microbial carbon and sulfur cycling in deeply buried ridge flank basalt. *Science* 339(6125):1305–1308.
6. Jungbluth SP, Grote J, Lin H-T, Cowen JP, Rappé MS (2013) Microbial diversity within basement fluids of the sediment-buried Juan de Fuca Ridge flank. *ISME J* 7(1):161–172.
7. Lavalleur HJ, Colwell FS (2013) Microbial characterization of basalt formation waters targeted for geological carbon sequestration. *FEMS Microbiol Ecol* 85(1):62–73.
8. Magnabosco C, et al. (2014) Comparisons of the composition and biogeographic distribution of the bacterial communities occupying South African thermal springs with those inhabiting deep subsurface fracture water. *Front Microbiol* 5:679.
9. Nyyssönen M, et al. (2014) Taxonomically and functionally diverse microbial communities in deep crystalline rocks of the Fennoscandian shield. *ISME J* 8(1):126–138.
10. Ben Maamar S, et al. (2015) Groundwater isolation governs chemistry and microbial community structure along hydrologic flowpaths. *Front Microbiol* 6:1457.
11. Labonté JM, et al. (2015) Single cell genomics indicates horizontal gene transfer and viral infections in a deep subsurface Firmicutes population. *Front Microbiol* 6:349.
12. Borgonie G, et al. (2015) Eukaryotic opportunists dominate the deep-subsurface biosphere in South Africa. *Nat Commun* 6:8952.
13. Borgonie G, et al. (2011) Nematoda from the terrestrial deep subsurface of South Africa. *Nature* 474(7349):79–82.
14. Biebl H, Pfenning N (1978) Growth yields of green sulfur bacteria in mixed cultures with sulfur and sulfate reducing bacteria. *Arch Microbiol* 117:9–16.
15. Morris BEL, Henneberger R, Huber H, Moissl-Eichinger C (2013) Microbial syntrophy: Interaction for the common good. *FEMS Microbiol Rev* 37(3):384–406.
16. Schink B, Stams AJM (2013) Syntrophism among prokaryotes. *The Prokaryotes*, eds Rosenberg E, DeLong EF, Lory S, Stackebrandt E, Thompson F (Springer, Berlin), pp 471–493.
17. Milucka J, et al. (2012) Zero-valent sulphur is a key intermediate in marine methane oxidation. *Nature* 491(7425):541–546.
18. McGlynn SE, Chadwick GL, Kempes CP, Orphan VJ (2015) Single cell activity reveals direct electron transfer in methanotrophic consortia. *Nature* 526(7574):531–535.
19. Wegener G, Krukenberg V, Riedel D, Tegetmeyer HE, Boetius A (2015) Intercellular wiring enables electron transfer between methanotrophic archaea and bacteria. *Nature* 526(7574):587–590.
20. Prokopenko MG, et al. (2013) Nitrogen losses in anoxic marine sediments driven by *Thioploca*-anammox bacterial consortia. *Nature* 500(7461):194–198.
21. Lau MCY, et al. (2014) Phylogeny and phylogeography of functional genes shared among seven terrestrial subsurface metagenomes reveal N-cycling and microbial evolutionary relationships. *Front Microbiol* 5:531.
22. Chivian D, et al. (2008) Environmental genomics reveals a single-species ecosystem deep within Earth. *Science* 322(5899):275–278.
23. Simkus DN, et al. (2016) Variations in microbial carbon sources and cycling in the deep continental subsurface. *Geochim Cosmochim Acta* 173:264–283.
24. Nealson KH, Inagaki F, Takai K (2005) Hydrogen-driven subsurface lithoautotrophic microbial ecosystems (SLiMEs): Do they exist and why should we care? *Trends Microbiol* 13(9):405–410.
25. Lippmann J, et al. (2003) Dating ultra-deep mine waters with noble gases and ^{36}Cl, Witwatersrand Basin, South Africa. *Geochim Cosmochim Acta* 67:4597–4619.
26. Lippmann-Pipke J, et al. (2011) Neon identifies two billion year old fluid component in Kaapvaal Craton. *Chem Geol* 283:287–296.
27. Sherwood Lollar B, et al. (2008) Isotopic signatures of CH_4 and higher hydrocarbon gases from Precambrian Shield sites: A model for abiogenic polymerization of hydrocarbons. *Geochim Cosmochim Acta* 72:4778–4795.
28. Moran MA, et al. (2013) Sizing up metatranscriptomics. *ISME J* 7(2):237–243.
29. Silver BJ, et al. (2012) The origin of NO_3^- and N_2 in deep subsurface fracture water of South Africa. *Chem Geol* 294-295:51–62.

30. Kojima H, Fukui M (2011) *Sulfuritalea hydrogenivorans* gen. nov., sp. nov., a facultative autotroph isolated from a freshwater lake. *Int J Syst Evol Microbiol* 61(Pt 7):1651–1655.
31. Kojima H, Fukui M (2010) *Sulfuricella denitrificans* gen. nov., sp. nov., a sulfur-oxidizing autotroph isolated from a freshwater lake. *Int J Syst Evol Microbiol* 60(Pt 12): 2862–2866.
32. Li L, et al. (2016) Sulfur mass-independent fractionation in subsurface fracture waters indicates a long-standing sulfur cycle in Precambrian rocks. *Nat Commun* 7:13252.
33. Lin LH, et al. (2006) Planktonic microbial communities associated with fracture-derived groundwater in a deep gold mine of South Africa. *Geomicrobiol J* 23:475–497.
34. Poser A, et al. (2014) Stable sulfur and oxygen isotope fractionation of anoxic sulfide oxidation by two different enzymatic pathways. *Environ Sci Technol* 48(16):9094–9102.
35. Onstott TC, et al. (2006) The origin and age of biogeochemical trends in deep fracture water of the Witwatersrand Basin, South Africa. *Geomicrobiol J* 23:369–414.
36. Meyerdierks A, et al. (2010) Metagenome and mRNA expression analyses of anaerobic methanotrophic archaea of the ANME-1 group. *Environ Microbiol* 12(2):422–439.
37. Haroon MF, et al. (2013) Anaerobic oxidation of methane coupled to nitrate reduction in a novel archaeal lineage. *Nature* 500(7464):567–570.
38. Magnabosco C, et al. (2016) The case for a dynamical subsurface ecosystem. bioRxiv: 040204.
39. Norlund KLI, et al. (2009) Microbial architecture of environmental sulfur processes: A novel syntrophic sulfur-metabolizing consortia. *Environ Sci Technol* 43(23):8781–8786.
40. Odum EP (2005) *Fundamentals of Ecology* (Thomson Brooks/Cole, Belmont, CA), 5th Ed.
41. Courchamp F, Berec L, Gascoigne J (2008) *Allee Effects in Ecology and Conservation* (Oxford Univ Press, New York).
42. Bosch J, Lee KY, Jordan G, Kim KW, Meckenstock RU (2012) Anaerobic, nitrate-dependent oxidation of pyrite nanoparticles by *Thiobacillus denitrificans*. *Environ Sci Technol* 46(4):2095–2101.
43. Guy BM, et al. (2012) A multiple sulfur and organic carbon isotope record from non-conglomeratic sedimentary rocks of the Mesoarchean Witwatersrand Supergroup, South Africa. *Precambrian Res* 216-219:208–231.
44. MacLean LCW, Pray TJ, Onstott TC, Southam G (2007) Mineralogical, chemical and biological characterization of an anaerobic biofilm collected from a borehole in a deep gold mine in South Africa. *Geomicrobiol J* 24:491–504.
45. MacLean LCW, et al. (2008) A high-resolution chemical and structural study of framboidal pyrite formed within a low-temperature bacterial biofilm. *Geobiology* 6(5):471–480.
46. Singh A, Wang H, Morrison W, Weiss H (2012) Modeling fish biomass structure at near pristine coral reefs and degradation by fishing. *J Biol Syst* 20:21–36.
47. Wang H, Morrison W, Singh A, Weiss H (2009) Modeling inverted biomass pyramids and refuges in ecosystems. *Ecol Modell* 220:1376–1382.
48. Anantharaman K, Breier JA, Sheik CS, Dick GJ (2013) Evidence for hydrogen oxidation and metabolic plasticity in widespread deep-sea sulfur-oxidizing bacteria. *Proc Natl Acad Sci USA* 110(1):330–335.
49. Hansen M, Perner M (2015) A novel hydrogen oxidizer amidst the sulfur-oxidizing *Thiomicrospira* lineage. *ISME J* 9(3):696–707.
50. Osburn MR, LaRowe DE, Momper LM, Amend JP (2014) Chemolithotrophy in the continental deep subsurface: Sanford Underground Research Facility (SURF), USA. *Front Microbiol* 5:610.
51. Orsi WD, Edgcomb VP, Christman GD, Biddle JF (2013) Gene expression in the deep biosphere. *Nature* 499(7457):205–208.
52. Edgar RC (2010) Search and clustering orders of magnitude faster than BLAST. *Bioinformatics* 26(19):2460–2461.
53. Abe T, et al. (2011) tRNADB-CE 2011: tRNA gene database curated manually by experts. *Nucleic Acids Res* 39(Database issue):D210–D213.
54. Abe T, et al. (2014) tRNADB-CE: tRNA gene database well-timed in the era of big sequence data. *Front Genet* 5:114.
55. Szymanski M, Barciszewska MZ, Erdmann VA, Barciszewski J (2002) 5S ribosomal RNA database. *Nucleic Acids Res* 30(1):176–178.
56. Quast C, et al. (2013) The SILVA ribosomal RNA gene database project: Improved data processing and web-based tools. *Nucleic Acids Res* 41(Database issue):D590–D596.
57. Grabherr MG, et al. (2011) Full-length transcriptome assembly from RNA-Seq data without a reference genome. *Nat Biotechnol* 29(7):644–652.
58. Robertson G, et al. (2010) De novo assembly and analysis of RNA-seq data. *Nat Methods* 7(11):909–912.
59. Simpson JT, et al. (2009) ABySS: A parallel assembler for short read sequence data. *Genome Res* 19(6):1117–1123.
60. Fu L, Niu B, Zhu Z, Wu S, Li W (2012) CD-HIT: Accelerated for clustering the next-generation sequencing data. *Bioinformatics* 28(23):3150–3152.
61. Hyatt D, et al. (2010) Prodigal: Prokaryotic gene recognition and translation initiation site identification. *BMC Bioinformatics* 11:119.
62. Edgar RC, Haas BJ, Clemente JC, Quince C, Knight R (2011) UCHIME improves sensitivity and speed of chimera detection. *Bioinformatics* 27(16):2194–2200.
63. Langmead B, Salzberg SL (2012) Fast gapped-read alignment with Bowtie 2. *Nat Methods* 9(4):357–359.
64. Camacho C, et al. (2009) BLAST+: Architecture and applications. *BMC Bioinformatics* 10:421.
65. Wiśniewski JR, Zougman A, Nagaraj N, Mann M (2009) Universal sample preparation method for proteome analysis. *Nat Methods* 6(5):359–362.
66. Nesvizhskii AI (2014) Proteogenomics: Concepts, applications and computational strategies. *Nat Methods* 11(11):1114–1125.
67. Moser DP, et al. (2003) Temporal shifts in microbial community structure and geochemistry of an ultradeep South African gold mine borehole. *Geomicrobiol J* 20:1–32.
68. Ward JA, et al. (2004) Microbial hydrocarbon gases in the Witwatersrand Basin, South Africa: Implications for the deep biosphere. *Geochim Cosmochim Acta* 68:3239–3250.
69. Sigman DM, et al. (2001) A bacterial method for the nitrogen isotopic analysis of nitrate in seawater and freshwater. *Anal Chem* 73(17):4145–4153.
70. Casciotti KL, Sigman DM, Hastings MG, Böhlke JK, Hilkert A (2002) Measurement of the oxygen isotopic composition of nitrate in seawater and freshwater using the denitrifier method. *Anal Chem* 74(19):4905–4912.
71. Granger J, Sigman DM (2009) Removal of nitrite with sulfamic acid for nitrate N and O isotope analysis with the denitrifier method. *Rapid Commun Mass Spectrom* 23(23): 3753–3762.
72. Purtschert R, et al. (2013) ^{81}Kr concentrations in deep fracture waters of the Witwatersrand Basin, South Africa (abs.). 23rd Goldschmidt Conference Italy, 25–30 August 2013. Available at goldschmidt.info/2013/abstracts/originalPDFs/5770.pdf. Accessed January 6, 2016.
73. Cussler EL (1984) *Diffusion: Mass Transfer in Fluid Systems* (Cambridge Univ Press, Cambridge, UK).
74. Tamimi A, Rinker EB, Sandal OC (1994) Diffusion coefficients for hydrogen sulfide, carbon dioxide, and nitrous oxide in water over the temperature range 293–368K. *J Chem Eng Data* 39:330–332.
75. Onstott TC (2005) Impact of CO_2 injections on deep subsurface microbial ecosystems and potential ramifications for the surface biosphere. *Carbon Dioxide Storage in Deep Geologic Formations for Climate Change Mitigation, Geologic Storage of Carbon Dioxide with Monitoring and Verification, The CO_2 Capture and Storage Project (CCP),* eds Thomas DC, Benson SM (Elsevier Publishing, Oxford, UK), pp 1217–1250.
76. Bethke CM (2008) *Geochemical and Biogeochemical Reaction Modeling* (Univ of Illinois, Urbana, IL), 2nd Ed.
77. Takahashi H, Seida Y, Yui M (2009) 3D X-ray CT and diffusion measurements to assess tortuosity and constrictivity in a sedimentary rock. *Diffus Fundam* 11:1–11.
78. Abiye TA, Mengistu H, Demlie MB (2011) Groundwater resource in the crystalline rocks of the Johannesburg area, South Africa. *J Water Resour Prot* 3:199–212.
79. Jin Q, Bethke CM (2003) A new rate law describing microbial respiration. *Appl Environ Microbiol* 69(4):2340–2348.
80. Jin Q, Bethke CM (2005) Predicting the rate of microbial respiration in geochemical environments. *Geochim Cosmochim Acta* 69:1133–1143.
81. Levchenko VV, Fleming R, Qian H, Beard DA (2010) An annotated English translation of 'Kinetics of stationary reactions' [M. I. Temkin, Dolk. Akad. Nauk SSSR. 152, 156 (1963)]. arXiv:1001.2861.
82. Otto R, Klont B, Konings WN (1985) The relation between phosphate potential and growth rate of *Streptococcus cremoris*. *Arch Microbiol* 142:97–100.
83. LaRowe DE, Helgeson HC (2007) Quantifying the energetics of metabolic reactions in diverse biogeochemical systems: Electron flow and ATP synthesis. *Geobiology* 5:153–168.
84. Thauer RK, Jungermann K, Decker K (1977) Energy conservation in chemotrophic anaerobic bacteria. *Bacteriol Rev* 41(1):100–180.
85. Tijhuis L, Van Loosdrecht MCM, Heijnen JJ (1993) A thermodynamically based correlation for maintenance gibbs energy requirements in aerobic and anaerobic chemotrophic growth. *Biotechnol Bioeng* 42(4):509–519.
86. Onstott TC, et al. (2014) Does aspartic acid racemization constrain the depth limit of the subsurface biosphere? *Geobiology* 12(1):1–19.
87. Hoehler TM, Jørgensen BB (2013) Microbial life under extreme energy limitation. *Nat Rev Microbiol* 11(2):83–94.
88. Davidson MM, et al. (2009) Sulfur isotope enrichment during maintenance metabolism in the thermophilic sulfate-reducing bacterium *Desulfotomaculum putei*. *Appl Environ Microbiol* 75(17):5621–5630.
89. Kelly DP (1999) Thermodynamic aspects of energy conservation by chemolithotrophic sulfur bacteria in relation to the sulfur oxidation pathways. *Arch Microbiol* 171:219–229.
90. Subletta KL (1987) Aerobic oxidation of hydrogen sulfide by *Thiobacillus denitrificans*. *Biotechnol Bioeng* 29(6):690–695.
91. Hoor AT (1976) Energetic aspects of the metabolism of reduced sulphur compounds in *Thiobacillus dentrificans*. *Antonie van Leeuwenhoek* 42(4):483–492.
92. Drobner E, Huber H, Rachel R, Stetter KO (1992) *Thiobacillus plumbophilus* spec. nov., a novel galena and hydrogen oxidizer. *Arch Microbiol* 157(3):213–217.
93. Smith RL, Ceazan ML, Brooks MH (1994) Autotrophic, hydrogen-oxidizing, denitrifying bacteria in groundwater, potential agents for bioremediation of nitrate contamination. *Appl Environ Microbiol* 60(6):1949–1955.
94. Strohm TO, Griffin B, Zumft WG, Schink B (2007) Growth yields in bacterial denitrification and nitrate ammonification. *Appl Environ Microbiol* 73(5):1420–1424.
95. Kristjansson JK, Schonheit P, Thauer RK (1982) Different Ks values for hydrogen of methanogenic bacteria and sulfate reducing bacteria—an explanation for the apparent inhibition of methanogenesis by sulfate. *Arch Microbiol* 131:278–282.
96. Sonne-Hansen J, Westermann P, Ahring BK (1999) Kinetics of sulfate and hydrogen uptake by the thermophilic sulfate-reducing bacteria *thermodesulfobacterium* sp. Strain JSP and *thermodesulfovibrio* sp. Strain R1Ha3. *Appl Environ Microbiol* 65(3):1304–1307.
97. Brysch K, Schneider C, Fuchs G, Widdel F (1987) Lithoautotrophic growth of sulfate-reducing bacteria and description of *Desulfobacterium autotrophicum* gen. nov., sp. nov. *Arch Microbiol* 148:264–274.
98. Widdel F, Pfennig N (1981) Studies on dissimilatory sulfate-reducing bacteria that decompose fatty acids. I. Isolation of new sulfate-reducing bacteria enriched with acetate from saline environments. Description of *Desulfobacter postgatei* gen. nov., sp. nov. *Arch Microbiol* 129(5):395–400.